Chinese Chemical Letters 33 (2022) 1650–1658

Contents lists available at ScienceDirect

Chinese Chemical Letters

journal homepage: www.elsevier.com/locate/cclet

Key progresses of MOE key laboratory of macromolecular synthesis and functionalization in 2020

Jie Ren, Xiao Shu, Ya Wang, Di Wang, Guangpeng Wu*, Xinghong Zhang*, Qiao Jin*, Jianzhao Liu*, Ziliang Wu*, Zhen Xu*, Chang-Zhi Li*, Hanying Li*

MOE Key Laboratory of Macromolecular Synthesis and Functionalization, Department of Polymer Science and Engineering, Zhejiang University, Hangzhou 310027, China

ARTICLE INFO

Article history:
Received 26 September 2021
Revised 14 October 2021
Accepted 19 October 2021
Available online 4 November 2021

Keywords:
Polymer
Catalyst
Drug nanocarrier
RNA methylation
Gel
2D Macromolecule
Organic optoelectronics

ABSTRACT

In 2020, the MOE Key Laboratory of Macromolecular Synthesis and Functionalization in Zhejiang University had made progresses in several aspects. First, a series of metal-free organoboron catalysts had been designed and synthesized facilely, exhibiting outstanding reactivity, thermalstability and productivity in different kinds of polymerization and cycloaddition reactions. Second, a variety of chalcogen (O, S, Se)-rich polymers had been synthesized *via* organocatalysis and fabricated to be the ionic conductive and photoluminescent materials. Third, diverse microenvironment-sensitive nanoparticles had been designed, and novel strategies had been realized, to enhance the therapeutic efficacy in cancer as well as biofilm-associated infections. Fourth, m6A modification on cellular transcriptome-wide messenger RNA had been successfully mapped at single base resolution using a metabolic labeling method. Fifth, a hydrogel-based robot had been developed, showing swift locomotion as a response to dynamic light stimulations. Sixth, the conformation-size scaling law and the conformation evolution map of 2D macromolecules in solution had been elucidated experimentally, in the single-layer graphene oxide model. Seventh, semitransparent polymer solar cells, promising as building-integrated photovoltaics, have been developed with the fine balance among power conversion efficiency, visible light transparency and infrared photon radiation rejection. Finally, long-range ordered bulk-heterojunctions of organic semiconductors had been achieved, and their superior optoelectronic properties and potential application in photoelectric conversion had been revealed. The related work progresses are reviewed in this paper.

1. Introduction

The MOE Key Laboratory of Macromolecular Synthesis and Functionalization was founded in 2005. The research of the whole laboratory mainly focuses on the fundamental and applied polymer science. Moreover, the laboratory is active in facilitating the development of industry-university cooperation to solve urgent technical needs of industry and to contribute to the sustainable development of the local and national economy. With the supports from polymer science disciplines and other related ones such as chemistry, material science and biology in Zhejiang University, five research directions of the laboratory have been established, including controlled catalytic polymerization, microstructure and rheology, photo-electro-magnetic functional polymers, biomedical functional polymers and separating functional polymers, to seek breakthrough in three main aspects. The first is the exploration of methods and mechanisms of controlled polymerization for the synthesis of novel functional polymers with controllable structures. The second is the study of structure-property relationship from the perspective of microstructure and rheology, to elucidate the formation and evolution of the morphology during the fabrication of polymers and their influences on the properties of the eventual functional materials. The third is the development of novel strategies for the construction of polymer-based functional materials, to achieve high-performance polymer materials or devices in a diversity of application fields.

In 2020, there had been abundant research achievements from the laboratory following the five research directions mentioned above, which were well-worthy to be highlighted. Therefore, we prepared this paper to review some of the frontier works published in 2020, in eight selected research directions involving metal-free organboron catalysts, chalcogen-rich polymers, drug nanocarriers, RNA modification, photoresponsive hydrogels,

* Corresponding authors.
E-mail addresses: gpwu@zju.edu.cn (G. Wu), xhzhang@zju.edu.cn (X. Zhang), jinqiao@zju.edu.cn (Q. Jin), liujz@zju.edu.cn (J. Liu), wuziliang@zju.edu.cn (Z. Wu), zhenxu@zju.edu.cn (Z. Xu), czli@zju.edu.cn (C.-Z. Li), hanying_li@zju.edu.cn (H. Li).

https://doi.org/10.1016/j.cclet.2021.10.052
1001-8417/

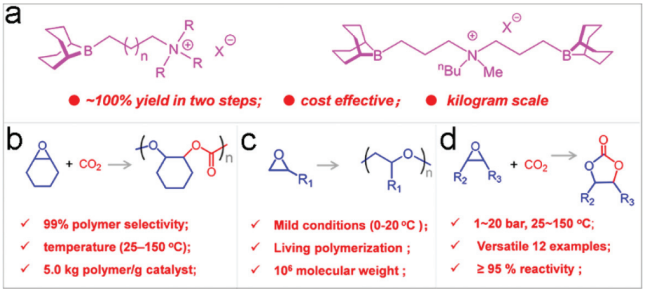

Fig. 1. (a) The chemical structures of organoboron bifunctional catalyst and their performances on (b) alternating copolymers of carbon dioxide and epoxides), (c) ring-opening polymerization of epoxides, and (d) cycloaddition of CO_2 and epoxides.

2D macromolecules, semitransparent organic solar cells and long-range ordered bulk-heterojunctions.

2. Scalable organoboron catalysts with unprecedented reactivity for synthesis of CO_2-polycarbonates, polyethers and cyclic carbonates

With the progress of human society, the development of green and efficient organic and polymeric catalysts to replace the existing metal catalysts for the preparation of fine chemicals and polymers, has become an inevitable trend in the development of chemistry [1]. Over the past decades, organocatalysis has evolved into one of the most powerful methodologies for its great potential for savings in cost, toxicity concerns, and reductions in chemical waste, regarding both in polymeric and organic chemistry [2].

Carbon dioxide (CO_2)-based polycarbonates (alternating copolymers of carbon dioxide and epoxides) [3], aliphatic polyethers (ring-opening polymerization of epoxides) [4] and cyclic carbonates (cycloaddition of CO_2 and epoxides) [5,6] are three typical representatives of traditional fine chemicals and polymer materials with a huge source of demand. Despite some organic catalysts have been successfully used in the synthesis of CO_2-based polycarbonates, aliphatic polyethers and cyclic carbonates, the catalytic efficiencies of these metal-free catalysts are still inferior to many state-of-the-art metal catalytic systems. In terms of the above problems, in 2020, we reported our efforts to synthesize a series of low-cost, high-activity organoboron catalysts that are expected to replace the current metal catalytic systems for the above three transformations [7–9]. We briefly summarize the performances for our catalysts in the following four conclusions (Fig. 1).

(1) Our organoboron catalysts were synthesized *via* a following quaterisation and hydroboration with a quantitative yield. The two-step reactions are really simple and efficient, meanwhile all the involved stocks are inexpensive and commercially available, enabling that kilogram-scale preparation of the catalyst could be conducted in laboratory (Fig. 1a).

(2) For the copolymerization of CO_2/cyclohexane oxide, our mononboric bifunctional catalysts showed the maximum working temperature at 150 °C, which is the highest record in the past more than half a century. Besides, the catalysts exhibited > 99% polymer selectivity and > 99% carbonate linkages under all the investigated reaction conditions (Fig. 1b). Notably, an efficiency of 5.0 kg of polymers/g of catalyst was achieved with a catalyst concentration of 50 ppm, which is the highest record achieved to date in all of the homogeneous catalyst-mediated copolymerization. On the basis of kinetic studies, control experiments, ^{11}B NMR investigation, crystal structure of catalyst, and density functional theory calculations, a novel polymerization mechanism was proposed and proved [7].

(3) For the ring-opening polymerization of propylene oxide and ethylene oxide, our diboric bifunctional catalysts are highly active (Fig. 1c). The living polymerization characteristics was determined by the systematical investigations of the relationship between the molecular weight of poly(propylene oxide) and the feed ratio, the relationship between the molecular weight of poly(propylene oxide) and conversion, and the chain extension experiment. In note, the catalyst loading can reduced to as low as 5 parts per million (ppm), giving efficiencies of 17.9 kg of poly(ethylene oxide)/g and 6.7 kg of poly(propylene oxide)/g of catalyst, respectively. On the basis of the control experiments, catalyst crystal structures, reaction kinetics and NMR investigation, an intramolecular ammonium cation-assisted S_N2 mechanism was first disclosed [8].

(4) For the cycloaddition of CO_2 and epoxides, our organoboron compounds displayed high activity towards a wide scope of cyclic carbonates (Fig. 1d). Importantly, our catalysts can withstand a high temperature up to 150 °C, rendering our organoboron catalysts to be one of the most efficient metal-free catalytic systems so far. In contrast to the current metal-free catalytic systems that involved using mol% catalyst loading, our catalyst showed an enhancement of three orders of magnitude (as high as 200,000/1 of epoxide/ catalyst, mole ratio). This performance greatly narrows the gap between the metal-free catalysts and the state-of-the-art metallic compounds [9].

In short, we designed a series of metal-free catalysts with facile preparation and unprecedented performances (reactivity, thermostability, and productivity). We hope the catalysts provided here hold promise in pushing the mentioned three transformations to the industry line. Besides, we also expect that these highly active metal-free boron catalysts should be useful for the developments in metal-residue-sensitive applications, such as lithography [10].

3. Chalcogen (O, S, Se)-rich polymers

Chalcogen (O, S, Se)-rich polymers are, of course, a family of low-carbon polymers. Because these polymers contain carbon-heteroatom (O, S, Se) groups such as (thio)ester, (thio)carbonate structures or even dynamic S-S, Se-Se bonds [11] in the backbone, chalcogen-rich polymers are often chemically recyclable in an upcycling manner, malleable for reuse. Especially, these polymers exhibit unique properties such as photoluminescence and ionic conductivity, and thus can be potentially applied as the display materials, battery materials, and biomaterials, and even biodegradable materials. We focus on using one-carbon compounds [CO_2, carbonyl sulfide (COS) and carbon disulfide (CS_2)] and cyclic anhydrides for synthesizing chalcogen-rich polymers. The discovery of organoboranes (*i.e.*, triethylborane, TEB, Fig. 2a) as the catalysts [12] lead to the successful syntheses of poly(thiocarbonate)s from the copolymerization of COS and epoxides [13,14], and polyesters from the copolymerization of cyclic anhydrides and epoxides [15]. The organoborane was also applied to the synthesis of polyethers from ring-opening polymerization of epoxides [16] for the first time, affording high molecular weight and narrow dispersity polyethers. These chalcogen-rich polymers have been demonstrated to be very promising as the ionic conductive [17] and photoluminescent [18] materials.

Inspired by the fact that most solid polymer electrolytes (SPEs) are prepared by blending oxygen-containing polymers with lithium salts, we developed a new SPE having high ionic conductivity and high mechanical strength. A poly(propylene monothiocarbonate)-*b*-poly(ethylene oxide) block copolymer (PPMTC-*b*-PEO) was synthesized in a controlled manner using TEB and quaternary onium salts as the catalysts. This block copolymer was then blended with bis(trifluoromethanesulfonyl) imide (LiTFSI) to afford SPE with separated phase structure. Being different to the previously reported

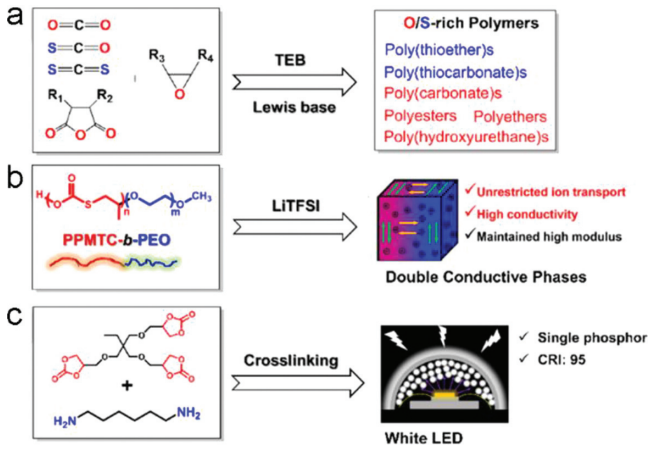

Fig. 2. (a) The synthesis of chalcogen (O, S)-rich polymers from C1 (anhydride) and epoxides through triethylborane catalysis (Se-containing monomer is not involved). Application of chalcogen (O, S)-rich polymers: (b) PPMTC-*b*-PEO/LiTFSI SPE with simultaneous improvement of ionic conductivity and mechanical properties. (c) Typical example of polymerization-induced emission: poly(hydroxyurethane) microsphere for white LED device.

SPEs, the $PPMTC_{17-59}$-*b*-PEO_{44}/LiTFSI (doping ratio of 1/3) electrolyte has a unique double conductive phase and exhibit high ionic conductivity of 2×10^{-4} S/cm at room temperature, and its storage moduli is *ca.* 1–4 orders of magnitude higher than that of the neat PEO/LiTFSI electrolyte. This work provides a double conductive phase strategy to simultaneous improvement of ionic conductivity and mechanical properties for making safety SPEs (Fig. 2b) [19]. In addition, we observed that the replacement of sulfur with selenium (Se) in polymer backbone can also lead to soft conductive materials. In 2020, we developed an easy-handled copolymerization route for synthesizing Se-rich polymers using γ-selenobutyrolactone and epoxides as the monomers under the catalysis of phosphazene base at 25 °C. The resultant poly(selenide-*alt*-ester)s had selenide and ester groups in each unit and well-controlled structure with >99% alternating degree, >99% Head-to-Tail diad content and hydroxyl terminals [20]. The blend of poly(γ-SBL-alt-PGE) with LiTFSI exhibited good ionic conductivity of 1.09×10^{-6} S/cm at 30 °C, close to the commercial PEG-based electrolytes (1×10^{-5} S/cm to 4×10^{-7} S/cm at room temperature). Of special, the refractive indices of the S and Se-rich polymers are usually high than 1.6, better than commercially available poly(carbonate)s (1.58) and poly(styrene) (1.59).

In very recent years, oxygen-rich polymers are revealed to be soft photoluminescent materials without nonconjugated structure. We collaborated with the Tang's group summarized the synthesis and properties of the unorthodox luminescent polymers [21]. These polymers generally possess oxygen-rich moieties such as ester, ether, hydroxyurethane units [22] with significant interactions of delocalized electrons within the aggregate of these groups. In this sense, polymerization, was proposed as an effective way to realize the fluorescence emission, that is, polymerization-induced emission (PIE). Therefore, in view of photoluminescence, PIE is a chemical process of transforming non-luminescent small molecules (*i.e.*, monomers) into luminescent polymers. Bear this concept in mind, a white-light-emitting poly(hydroxyurethane) microsphere without non-conjugated structure were successfully prepared from the crosslinking reaction of trimethylolpropane tri(cyclic carbonate)ether and 1,6-hexanediamine in chloroform (Fig. 2c). It was proposed that multiple n–π^* transitions *via* through-space conjugation of the carbamate group aggregate leads to the white light emission. This material was fabricated to be a white light-emitting diode (LED) with a high color rendering index (CRI) of 95, suggesting excellent color rendering for wide application [23].

Responding to the call of sustainable society development, chalcogen-rich polymers have attracted people's attention. Our work shows that these polymers have specific properties, such as the abovementioned electrical and optical properties. Of importance, these chalcogen-rich polymers are low-carbon in composition and will be sustainable materials. The carbon-heteroatom structures which are more polar and weaker than carbon-carbon bond, providing opportunities toward the design and synthesis of sustainable polymers with various possible structures [24].

4. Drug nanocarriers targeting to pathological tissue microenvironment

During the progression of diseases, pathological tissues will form specific pathological microenvironment due to pathogen proliferation, abnormal metabolism, pathological inflammation, *etc.* The specific pathological tissue microenvironment can reduce drug bioavailability and induce drug resistance, thus significantly restricting the therapeutic efficacy. How to design emerging drug nanocarriers to overcome the dilemma of pathological tissue microenvironment is still a big challenge. On one hand, we could take advantage of the specific pathological tissue microenvironment to design stimuli-sensitive drug nanocarriers to realize targeted drug accumulation and smart drug release, leading to enhanced drug bioavailability and improved pharmacodynamics [25–28]. On the other hand, we could remodel pathological tissue microenvironment to sensitize the drugs and improve therapeutic efficacy [29,30].

Tumor tissue exhibits the signature of specific microenvironment, including lowing pH, hypoxia, overexpressed enzymes, and so on [31]. The specific microenvironment can be used as a trigger to fabricate stimuli-sensitive drug nanocarriers. For example, we designed matrix metalloproteinase-2 (MMP-2) sensitive stealth peptide-detachable supramolecular aggregation-induced emission (AIE) nanocarriers for image-guided drug delivery [32]. The nanocarriers could achieve simultaneous long circulation time, enhanced cell uptake, and on-demand drug release due to the programmed stimuli-responsive behavior. The remodeling of tumor microenvironment is an emerging strategy to enhance the therapeutic efficacy. As an example, the hypoxic tumor microenvironment is a large obstacle in photodynamic therapy [33]. In order to relieve the hypoxic tumor microenvironment, the respiration inhibitor 3-bromopyruvate (3BP) was integrated into the supramolecular photosensitizer nanocarriers [34]. 3BP could not only relieve the hypoxic tumor microenvironment by reducing oxygen consumption, but also induce pro-death autophagy, leading to enhanced photodynamic therapy and efficient tumor regression. It is one of the very few examples that the hypoxic microenvironment could be relieved by the decrease of oxygen consumption.

Effective drug penetration is a critical step in drug delivery which may result in the failure of cancer chemotherapy [35]. Especially, pancreatic tumor tissue is rich in desmoplastic stroma which forms a natural physical barrier of drug penetration. In order to overcome the dense stroma barrier, we reported an effective two-step delivery strategy by sequential delivery of metformin (MET) and pH-sensitive gemcitabine (GEM) nanocarriers (Fig. 3) [36]. MET could inhibit the secretion of TGF-β by pancreatic cancer cells, leading to the deactivation of pancreatic stellate cells (PSCs). Therefore, the secretion of α-SMA and collagen by PSCs could be inhibited, resulting in the depletion of the dense stroma, which greatly improved the penetration ability of GEM nanocarriers. The therapeutic efficacy of GEM nanocarriers could then be significantly improved. Similarly, the penetration ability of GEM nanocar-

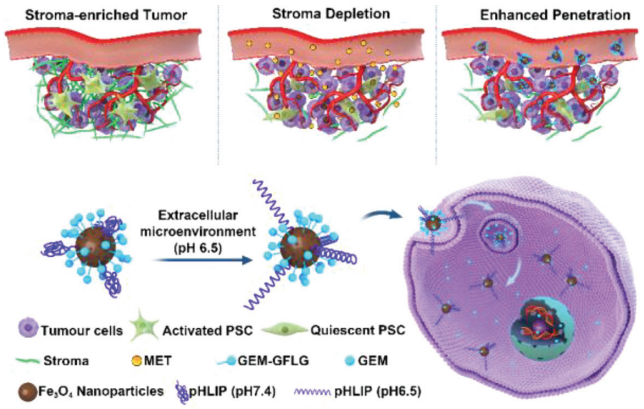

Fig. 3. Illustration of MET-induced stromal depletion for enhancing the penetration of pH-sensitive GEM nanocarriers. Reproduced with permission [36]. Copyright 2020. American Chemical Society.

riers could also be improved after stromal depletion by nitric oxide nanocarriers [37].

Similar to tumor microenvironment, bacterial biofilms also behave specific microenvironment (low pH, overexpressed enzymes, hypoxia, quorum sensing, *etc.*), which could be utilized to fabricate drug delivery systems for enhanced drug penetration, retention, and release [38,39]. We designed size and charge adaptive acidic biofilm microenvironment-sensitive azithromycin (AZM)-conjugated clustered nanoparticles (AZM-DA NPs) for the treatment of biofilm-associated infections [40]. AZM-DA NPs were disassembled in acidic biofilm microenvironment (pH 6.0), resulting in the release of AZM-conjugated poly(amidoamine) dendrimer (PAMAM). The released AZM-conjugated PAMAM was positively charged with very small size, which could be effectively penetrated into biofilms and adhered to bacterial cells, leading to enhanced permeabilization of the bacterial membrane and increased AZM internalization. It was interesting to show that AZM-DA NPs exhibited much better antibiofilm activities than free AZM. More importantly, AZM-DA NPs could reduce the occurrence of drug resistance since the dose of AZM was remarkably reduced. The outstanding antibiofilm capability of AZM-DA NPs was further confirmed by a mouse chronic lung infection model. The biofilm hypoxia was proved to be closely related with antibiotic resistance [41]. In order to address this issue, we proposed an innovative strategy to enhance the therapeutic efficacy of conventional antibiotics by relieving biofilm hypoxia [42]. Perfluorohexane (PFH)-loaded liposomes were used as oxygen carriers to relieve biofilm hypoxia. PFH loaded liposomes could effectively relieve biofilm hypoxia, accompanied with the down-regulation of multiple drug resistant genes related with drug efflux pumps and quorum sensing. The bactericidal ability of multiple antibiotics including aztreonam, ceftazidime, and piperacillin-tazobactam was greatly improved. The relief of biofilm hypoxia could be considered as a new paradigm for enhanced antibiotic therapy in combating biofilm-associated infections.

5. Decoding macromolecular messenger rna m^{6}A methylation at single base resolution

As a biological macromolecule, RNA is commonly known to contain four basic nucleoside monomer units, A, U, C, G. However, in recent years, more than 170 types of natural RNA chemical modifications have been discovered, which plays important roles in the biological processes [43,44]. *N*^{6}-methyladenosine (m^{6}A) is the most prevalent internal modification in mammalian messenger RNA (mRNA), and regulates gene expression by its specific methyltransferases (writers) [45–47], demethylases (erasers) [48,49] and binding proteins (readers) [50]. In order to understand the functions of m^{6}A in mRNA, identification of their accurate locations on mRNA is highly necessary and important. However, transcriptome-wide mapping of m^{6}A at base resolution remains an issue. In the field, a few tools have been tried to address this issue. The traditional detection methods of mRNA m^{6}A are based on m^{6}A antibody immunoprecipitation (IP) and high-throughput sequencing (m^{6}A-seq [51], MeRIP [52]), which limits the resolution to 100–200 nucleotides mapping window. To increase the resolution, photo-crosslinking technologies were combined with IP (PA-m^{6}A-seq [53], miCLIP [54]), and similarly, m^{6}A-binding protein was also employed to fuse with cytidine deaminase (DART-seq [55]). However, the m^{6}A sites are identified in an indirect way, possibly leading to a bias of detection. Also, antibody-independent enzymatic methods were developed, such as m^{6}A-sensitive RNA-endoribonuclease-based sequencing m^{6}A-REF-seq [56] and MAZTER-seq [57], which are limited in the scope of working substrate sequences.

We developed a metabolic labeling method, 'm^{6}A-label-seq', to detect mRNA m^{6}A transcriptome-wide at single base resolution [58]. We consider the cellular origin of methyl group for mRNA methylation, which comes from amino acid methionine, a precursor of methylase cofactor *S*-adenosyl methionine (SAM). We aimed to replace methyl with a post-modifiable group for the purpose of detection. We synthesized a methionine analog Se-allyl-L-selenohomocysteine, and thought that it could lead to the substitutions of methyl group and *S* atom on SAM with allyl and Se, respectively, through the cellular metabolic processes. After human and mouse cells were fed with this molecule, the allyl group could indeed be transferred to the supposed mRNA m^{6}A-forming sites to form *N*^{6}-allyladenosine (a^{6}A), instead of m^{6}A (Figs. 4a and b). Then, we used a^{6}A-antibody-based enrichment to purify a^{6}A-modified mRNA from cells. After mild iodination treatment, a^{6}A could be transformed into 1,*N*^{6}-cyclized adenosine (cyc-A), which is able to induce base misincorporation during reverse transcription of RNA into complementary DNA (cDNA) (Fig. 4c). Combined with high-throughput sequencing of cDNA and bioinformatic analysis, we identified a few thousand mRNA m^{6}A sites in human HeLa, HEK293T and mouse H2.35 cells. The enrichment profiles of a^{6}A peak show a high similarity to common cellular m^{6}A distribution pattern with a peak near stop codon (Fig. 4d). The reads with A to C/T/G mutations are featured with GGAC sequence in agreement with the previously reported m^{6}A consensus motif (Fig. 4e). Our method overcomes the limitations of currently available m^{6}A detection methods, offers advantages in detecting clustered m^{6}A sites, and holds promise to locate nuclear nascent RNA m^{6}A modifications. This method also provides new ideas of combining metabolic labeling and post-chemical treatment to detect other chemical modifications on biomacromolecules.

6. Light-steered locomotion of anisotropic hydrogels

Fascinated by the capacities of living organisms to navigate through challenging environments by versatile deformations and motions, designing bioinspired/biomimetic soft actuators and robots has raised extensive interest in recent years due to their promising applications in biomedical and engineering fields [59–61]. Hydrogels are recognized as an ideal material to investigate the basic principle for programmable morphing/motion and to construct soft actuators/robots, considering the multiple responsivity to external stimuli and similarity to soft biotissues [62–65]. Although rapid progress has been achieved in understanding the relationship between the structure features and morphing abilities of natural and artificial materials, it still remains a big challenge to develop hydrogel-based soft robots with elaborate structures and multi-gait locomotion. The difficulties include (i) lacking muscle-like hydrogels to serve as the motor and generate re-

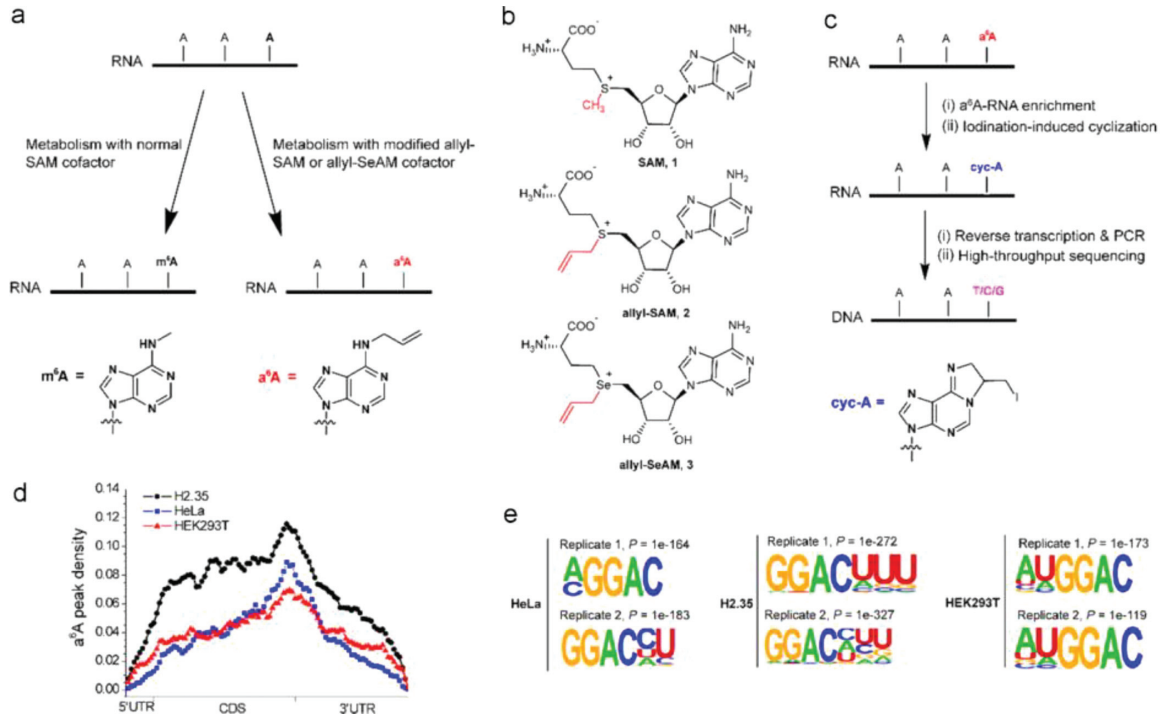

Fig. 4. (a) A schematic illustration of metabolic labeling of the supposed m^{6}A site with a^{6}A using an allyl-SAM (SeAM) cofactor. (b) The chemical structures of SAM, allyl-SAM and allyl-SeAM. (c) A simplified procedure to locate metabolically labeled a^{6}A, transcriptome-wide, at single base resolution. (d) Profiles of a^{6}A peak density along mRNA transcripts. (e) Consensus motifs for the sequences containing A-to-C/T/G mutations. $n = 2$ biologically independent samples. Reproduced with permission [58]. Copyright 2020, Nature Publishing Group.

versible, anisotropic deformations, (ii) low response speed of the gel limited by molecular diffusion, (iii) absence of efficient strategies to convert cyclic deformations into directional locomotion.

Recently, we developed a hydrogel-based soft robot, capable of swift locomotion under dynamic light stimulations (Fig. 5) [66,67]. A muscle-like hydrogel was fabricated by electric-field-induced orientation of nanosheets (NSs), which were immobilized by photopolymerizing a precursor solution in the presence of gold nanoparticles. Hydrogels with sophisticated ordered structures can be developed by multi-step electrical orientation and photolithographic polymerization (Figs. 5a and b). The obtained monodomain poly(*N*-isopropylacrylamide) (PNIPAm) hydrogel showed fast and reversible anisotropic deformation upon heating or light irradiation. It readily expanded to 1.5 times in the direction perpendicular to the alignment of NSs, while contracted to 0.8 in the direction parallel to the alignment of NSs. The isochoric deformation stemmed from the temperature-mediated permittivity of the media due to the dehydration of PNIPAm, which modulated the electrostatic repulsion between the highly charged NSs [68,69]. Crawling motion of the anisotropic gel was achieved by scanning of a light beam (520 nm), which induced traveling contraction and dynamic undulation of friction coefficient of the gel against a hydrophobic substrate (Figs. 5c and d). The variation of friction coefficient arose from the enhanced hydrophobicity of the gel matrix at elevated temperature [70]. The spatiotemporal actuation of the gel resulted in synchronized travelling deformation and anchoring, and thus directional crawling of the gel. Other motion gaits such as walking and turning can also be realized by designing the patterns of the gel and manipulating the light actuation. As shown in Fig. 5e, light scanning from left to right directed the travelling bending, dynamic friction, and hence walking motion of the stripe-patterned gel [71–74]. Sequential scanning with controlled direction led to continuous walking of the gel (Fig. 5f). Since the locomotion was achieved by friction control in a dynamic way (Fig. 5g), the motion direction can be easily switched by the scanning direction of the light. Turning motion was also realized in this gel by light scanning at an oblique angle relative to the slender gel. The working principle of self-coordinated shape change and friction modulation should merit the developments of continuum soft robots with specific applications [75–77].

7. Conformation engineering of 2D macromolecular graphene oxide

Two-dimensional sheets with 2D topology have emerged as a new member of macromolecules after the classic 1D linear counterpart and are posing to rapidly extend material technologies [78–80]. 2D macromolecules have rich properties that cover from insulator to semiconductor and metal, promising their great use values for many applications. The great expectations of 2D macromolecules urgently call not only a unified understanding of their macromolecular behavior in the new 2D topology but also a general methodology to guide the precise fabrication to achieve disruptive performances of their macroscopic materials. Since 1980s, theoretic researches have depicted the basic statistical mechanics of membranes and tethered surface [81–85]. However, the unification between theoretical predictions and experiments still needs to be verified and characteristic 2D features are waiting to be unveiled.

Recently, we revisited the conformation issue of 2D macromolecules in experiments. We chose single layer graphene oxide (GO) sheets as the experimental model, which can be well-controlled in size and also can eliminate the possible experimental errors caused by the wide distribution in thickness. Based on this thought flow, two major advances have been achieved so far [86–88].

The first issue of conformations of 2D macromolecules is the size related scaling law in solutions, which has been long debated

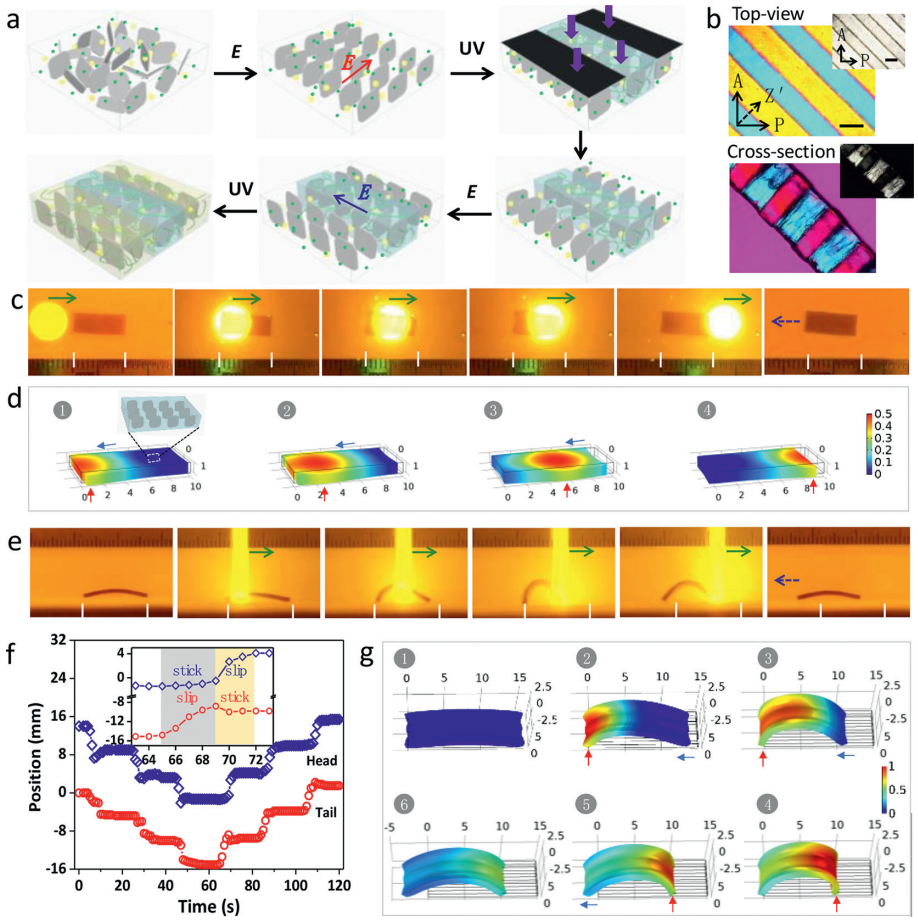

Fig. 5. (a) Preparation of patterned hydrogels by multi-step electrical orientation of the nanosheets and photolithographic polymerization of a precursor solution in the presence of gold nanoparticles. (b) Polarizing microscope images of the stripe-patterned hydrogel. Scale bar: 1 mm. (c, d) Snapshots of crawling motion of a slender monodomain gel under the scanning of a light beam (c) and numerical simulation to show the crawling kinematics (d). (e-g) Snapshots of walking motion of the stripe-patterned gel (e), displacements of the head and tail of the gel under cyclic light scanning (f), and numerical simulation to show the walking kinematics (g). Green and blue arrows in (c, e) indicate the light scanning direction and motion direction, respectively. Red and blue arrows in (d, g) indicate the anchoring spot and motion direction of the gel. Reproduced with permission [66]. Licensed under CC-BY.

for nearly 40 years [84,85]. We experimentally validate the scaling relation between conformation and size, by testing dynamic parameters of GO solutions [86]. Using Ubbelohde capillary rheology, we determined the Flory-type and Mark–Houwink–Sakurada scaling rules in the self-avoiding, good-solvent regime through the critical overlapping concentration ($C^* \sim L^{-0.87}$, L is the lateral size) and intrinsic viscosity ($[\eta] \sim M^{\alpha}$, $\alpha = 0.33$, M is the molecular weight). The measured Flory exponent $\gamma = 0.87$ is well located between self-avoiding (4/5) and rigid (1) limit, indicating a nearly flat conformation with out-of-plane ripples caused by thermal fluctuation (Fig. 6a). The dimensional constraint of 2D macromolecules results their smaller α value in the Mark-Houwink scaling relation than the value of ordinary linear chains (0.5–0.8), as shown in Fig. 6b. The experimental validation of the conformational scaling law of 2D GO directs a general theoretic framework to include the two-dimensional topology of macromolecules and underpins the systematic guidance for the description, design, and engineering of 2D macromolecules.

To date, diverse conformational phases of 2D macromolecules have been predicted in theory but remain unclear in experimental validation. By tuning the solvent property and the interaction between GO sheets, we systematically investigated the conformation evolution from the basic flat one. We concluded a conformational phase map of 2D macromolecules in solution in the GO model (Fig. 6c). The map covers not only predictable intramolecular phases but also intermolecular behaviors beyond theoretical prediction [87]. A symmetry-selection rule behind the conformation transition has been concluded, that discriminates anisotropic one-dimensional folding and isotropic 3D crumpling phases determined by the surface interaction. These symmetry-selective behaviors indicate a strong path-dependent competition between the elastic distortion and surface adhesion. The phase map offers a unified description of the conformational behaviors of 2D macromolecules that bridges the gap between theories and experiments, as well as a general guidance to precisely control multiscale condensed conformations of 2D nanomaterials.

By seizing the conformation of 2D macromolecules, we proposed a conceptually new methodology, named as conformation engineering of 2D sheets, extending from the single sheet behavior and liquid crystals, to the condensed state and macroscopic materials [88]. The “conformation engineering” concept starts to establish a unified theory of 2D polymers after the classic 1D antiquity and should become a systematic guidance to precisely control the multiscale structures of macroscopic materials of graphene and other 2D macromolecules [89–92].

8. High-performance semitransparent polymer solar cells

Despite the remarkable performance progress being made, efforts are still needed to push polymer solar cells (PSCs) to-

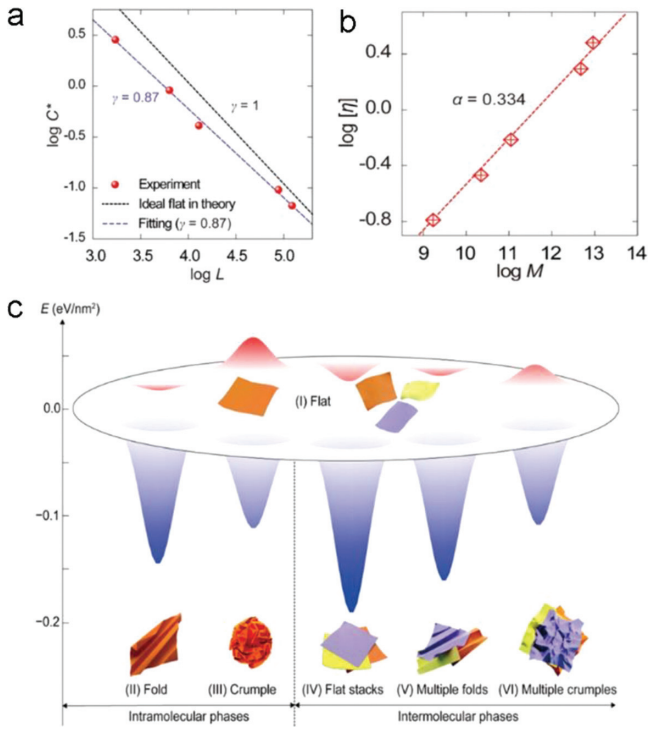

Fig. 6. (a) The scaling relation between overlapping transition concentration and the molecular size of single layer GO sheets in good solvent. (b) The scaling relation between the intrinsic viscosity and the molecular weight of GO sheets. Reproduced with permission [86]. Copyright 2020 American Chemical Society. (c) The established conformation transition map of 2D macromolecules, as concluded from the experimental observations of conformation transition of single layer GO and coarse grain simulations. Reproduced with permission [87]. Copyright 2020, Cell Press.

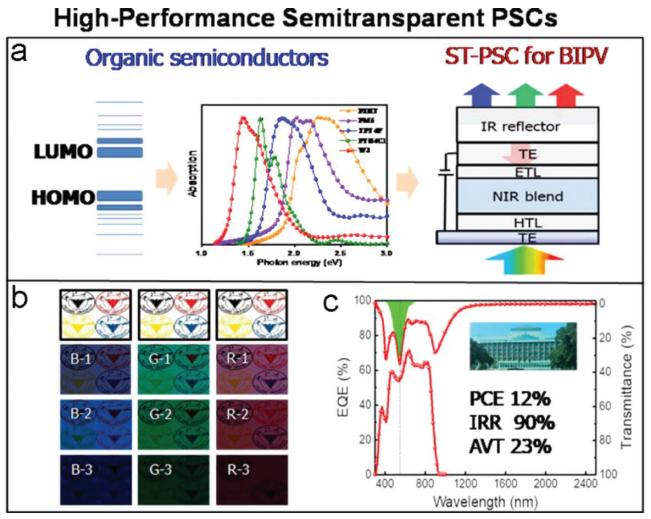

Fig. 7. (a) Schematic diagram of optoelectronic properties of organic semiconductors and semitransparent polymer solar cells for BIPV application. (b) Pictures of Zhejiang University logos under the different transmittance spectra of ST-PSCs. Reproduced with permission [98]. Copyright 2020, American Chemical Society. (c) Transmittance and EQE spectra of ST-PSCs based on NIR ternary blends with promising features of power generation, see-through and infrared reflection. Reproduced with permission [99]. Copyright 2020, Wiley-VCH.

ward practical relevance [93–95]. Semitransparent PSCs (ST-PSCs) can open up the promising photovoltaic application as building-integrated photovoltaics (BIPVs) [96–101]. They leverage the unique advantages of organic semiconductors, such as lightweight and solution-processable, and ease tuning of optoelectronic properties, which enable PSCs [102–110], differing from inorganic photovoltaics, with great potentials to function as see-through power windows (Fig. 7a). Yet, there remain significant challenges for ST-PSCs utilize the spectrally engineered photons for fine balancing device parameters of power conversion efficiency (PCE), average visible transparency (AVT) and infrared photon radiation rejection (IRR).

Recently, we have demonstrated new designs of multifunctional ST-PSCs through the rational integration of organic photoactive layers, transparent electrode and infrared photon reflector, exhibiting near 30% AVT and PCE of 7.3%, as well as an excellent IRR of over 93% (780–2500 nm), with promising perspective for window application [97]. ST-PSCs with vivid colors are also successfully demonstrated by employing a Fabry–Pérot electrode, to obtain PCE of >14% and maximum transmittance up to 31% (Fig. 7b) [98]. With further employing ternary blends with alloy-like near-infrared (NIR) acceptors, ST-PSCs exhibit the improved photovoltaic efficiency while remaining visible absorption unchanged, leading to not only perfect fitting of visible transmittance peak (555 nm) with the photopic response of the human eye but also excellent IRR of 90% (780–2500 nm), along with 23% AVT and over 12% PCE (Fig. 7c) [99]. To our knowledge, this is the best-performed multifunctional ST-PSCs with desirable functions of power generation, infrared reflection, and see-through, as power window. These efforts provide effective methodologies to access PSCs with promising perspectives as BIPVs.

9. Bulk-heterojunction with long-range ordering

"Long-range ordering" and "heterojunction" are two of the key structural factors for organic optoelectronics. On one hand, in comparison of short-range ordering in amorphous or polycrystalline states, "long-range ordering" in single-crystalline organic semiconductors always leads to improved properties of carrier transport (mobility) [111,112], as well as exciton diffusion [113]. On the other hand, "heterojunction" guarantees exciton dissociation [114] in photoelectric conversion materials, by virtue of the formation of interfaces. More importantly, it has been demonstrated that charge separation at interface can be benefit by ordering [115]. Thus, long-range ordered heterojunctions can be ideal active materials for organic optoelectronic devices given by the comprehensively enhanced photoelectric processes including exciton diffusion and dissociation, as well as subsequent charge generation and motion toward electrodes. However, in contrast to single-crystalline planar heterojunctions [116], it is difficult to achieve long-range ordering in bi-continuous bulk-heterojunctions (BHJs, Fig. 8a), which have been widely used in organic photovoltaics [97] or photodetectors [117] because of the abundant interface. Essentially, due to the enormous nucleation events occurred inside the conventional donor-acceptor blends, only short-range ordered BHJs (Fig. 8b) have been fabricated. This non-ideal crystallization kinetics limits the further development of photoelectric conversion devices.

Inspired by the biominerallization strategy by which guest materials are incorporated into host single crystals, single-crystals were grown from hydrogels and gel-networks were found to be incorporated inside the single-crystals, forming 3D interpenetration structure without any interruption to the single-crystallinity [118]. Accordingly, instead of the conventional one-step fabrication where bi-continuous structure was formed from spontaneous phase-separation during blending, recently [119], we achieved BHJs with long-range ordering following the two-step gel-method (Fig. 8c). First, 3D networks of poly[2-methoxy-5-(2-ethylhexyloxy)-1,4-phenylenvinylene] (MEH-PPV) were constructed by gelation in organic solvents that contain C_{60} solutes. Subsequently, C_{60} single-crystals with hexagonal bipyramid configuration (Fig. 8d) were gently grown inside the MEH-PPV gels by dif-

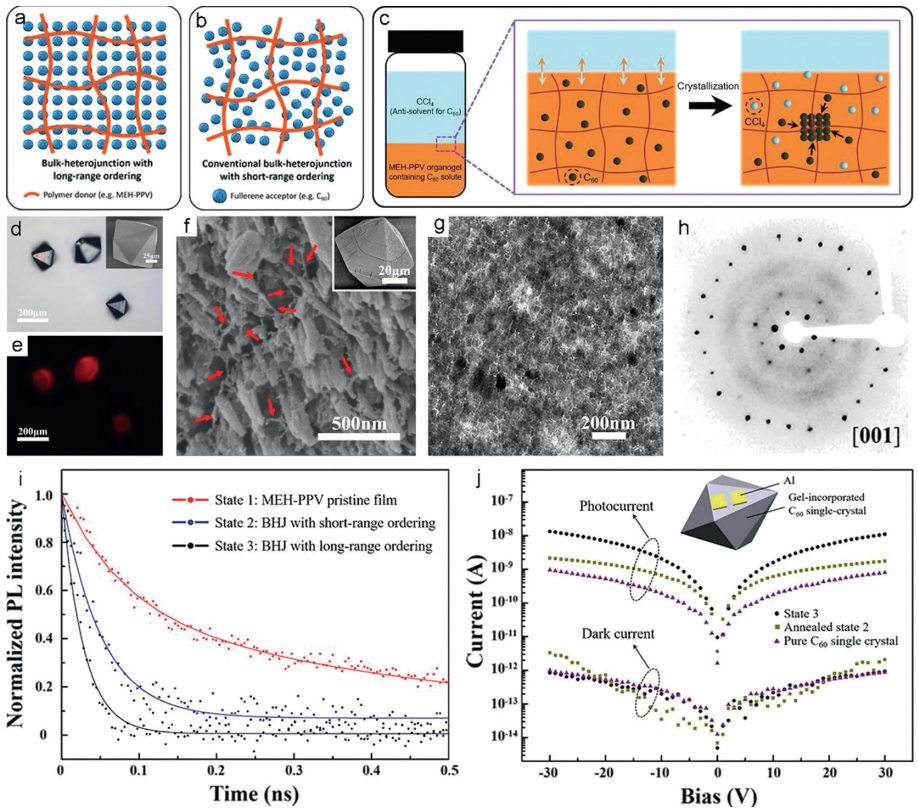

Fig. 8. (a, b) Schematic illustrations of BHJs with long-range (a) and short-range (b) ordering. (c) A schematic representation of a C_{60} crystal growing inside MEH-PPV gel. (d) An optical microscope (OM) image of gel-grown crystals. Inset: A scanning electron microscope (SEM) image of a gel-grown crystal. (e) A fluorescent OM image of the MEH-PPV gel blocks left after selective dissolution of C_{60} hosts. (f) A SEM image of an etched gel-grown crystal. The red arrows highlight the exposed MEH-PPV fibers. Inset: Full view of the etched crystal in SEM. (g) The transmission electron microscope (TEM) image of an ultra-thin section of a gel-incorporated crystal. (h) A X-ray diffraction pattern of a gel-incorporated crystal viewed from c-axis. (i) PL lifetimes of pristine MEH-PPV film (state 1), conventional blends (state 2) and gel-incorporated single-crystal (state 3). (j) Photocurrent of photoresistors based on state 3, annealed state 2 and pure C_{60} single-crystal. Reproduced with permission [119]. Copyright 2020. American Chemical Society.

fusion of anti-solvents. Consequently, MEH-PPV was incorporated inside the entire C_{60} crystal, evidenced by the residues of shape-resembled fluorescent gel blocks after selectively dissolving the C_{60} hosts (Fig. 8e). Furthermore, fibrous MEH-PPV were exposed after slightly etching the crystal surface (Fig. 8f), and random networks were observed in an ultra-thin slice of a crystal (Fig. 8g), revealing the 3D interpenetration structure between this typical donor-acceptor pair [120] and hence the formation of BHJs. More importantly, the long-range ordering of gel-incorporated crystals was indicated by single-crystal X-ray diffraction, exhibiting a single set of diffraction pattern viewed from c-axis (Fig. 8h). Finally, we examined their optoelectronic properties, showing an improved efficiency of charge-transfer with nearly a half decrease in photoluminescence (PL) lifetime (Fig. 8i), as well as enhanced photodetection with an over 5 times increase in photoresponsivity (Fig. 8j), in comparison with short-range ordered blends [119].

The bio-inspired gel-incorporation strategy essentially overcomes the limitation in the degree of ordering, and hence the long-range ordered BHJs show great potential in photoelectric conversion devices. Moreover, it provides a unique platform to deepen the fundamental knowledge about the photopysical processes that exist in organic heterojunctions, such as charge delocalization [121] at interface region or recombination caused energetic loss [93,122,123], owing to the lack of interference from structural or energetic disorder. Nevertheless, no matter for device fabrication or advanced photophysical characterizations, organic semiconductors are generally processed with nanometer-sized thickness. Thus, massive efforts are still required in thinning the bulky crystals, as well as in expanding the scope of crystalline host materials toward non-fullerene acceptors [103,105,108] and even perovskites [124–126].

9. Conclusion

In summary, we briefly reviewed the 2020-published key progresses in eight selected research directions of the MOE Key Laboratory of Macromolecular Synthesis and Functionalization, Zhejiang University. The first is the design of novel metal-free organoboron catalysts, which show outstanding catalysis performance (reactivity, thermalstability and productivity). The second is the synthesis of chalcogen-rich polymers and their functionalization toward ionic conductivity and photoluminescence. The third is the design of polymer-based nanoparticles and novel strategies for the therapy of cancer and biofilm-associated infections. The forth is the achievement of transcriptome-wide mapping of RNA m^6A modification at single base resolution. The fifth is the development of a polymer hydrogel-based robot that show spontaneous locomotion induced by dynamic light stimulations. The sixth are the experimental elucidations of conformation-size scaling law and the conformation evolution map of 2D macromolecules in solution. The seventh is the precise fabrication of semitransparent polymer solar cells toward building-integrated photovoltaics. The final is construction and consequent optoelectronic properties of long-range ordered bulk-heterojunction inspired by a unique biomineralization strategy. We believe that these achievements and scientific views would facilitate the following-up researches in the synthesis, physics and applications of novel functional polymers.

Declaration of competing interest

The authors declare that they have no known competing financial interests or personal relationships that could have appeared to influence the work reported in this paper.

Acknowledgment

The authors acknowledge the support from the SCI-TECH Academy of Zhejiang University.

References

[1] M. Hong, J. Chen, E.Y.X. Chen, Chem. Rev. 118 (2018) 10551–10616.
[2] Y. Lin, J. Yu, X. Zhang, et al., Chin. Chem. Lett. 33 (2022) 186–196.
[3] Y.F. Liu, K.L. Huang, D.M. Peng, et al., Chin. Chem. Lett. 18 (2007) 209–212.
[4] Y.J. Huang, X.H. Zhang, Z.J. Hua, G.R. Qi, Chin. Chem. Lett. 21 (2010) 897–901.
[5] F.W. Chen, T. Dong, X.F. Li, et al., Chin. Chem. Lett. 22 (2011) 871–874.
[6] M.U. Khan, S.U. Khan, J. Kiriratnikom, et al., Chin. Chem. Lett. 33 (2022) 1081–1086.
[7] G.W. Yang, Y.Y. Zhang, R. Xie, G.P. Wu, J. Am. Chem. Soc. 142 (2020) 12245–12255.
[8] G.W. Yang, Y.Y. Zhang, R. Xie, G.P. Wu, Angew. Chem. Int. Ed. 59 (2020) 16910–16917.
[9] Y.Y. Zhang, G.W. Yang, R. Xie, et al., Angew. Chem. Int. Ed. 59 (2020) 23291–23298.
[10] R.M. Jacobberger, V. Thapar, G.P. Wu, et al., Nat. Commun. 11 (2020) 4151.
[11] J. Xia, T. Li, C. Lu, H. Xu, Macromolecules 51 (2018) 7435–7455.
[12] Y. Wang, J.L. Yang, C.J. Zhang, X.H. Zhang, Acta Polym. Sin. 51 (2020) 1092–1103.
[13] J.L. Yang, H.L. Wu, Y. Li, et al., Angew. Chem. Int. Ed. 56 (2017) 5774–5779.
[14] C.J. Zhang, H.L. Wu, Y. Li, et al., Nat. Commun. 9 (2018) 2137.
[15] L.F. Hu, C.J. Zhang, H.L. Wu, et al., Macromolecules 51 (2018) 3126–3134.
[16] C.J. Zhang, H.Y. Duan, L.F. Hu, et al., ChemSusChem 11 (2018) 4209–4213.
[17] B. Zhao, X. Lu, Q. Wang, et al., Chin. Chem. Lett. 31 (2020) 831–835.
[18] Z. Fu, K. Wang, B. Zou, Chin. Chem. Lett. 30 (2019) 1883–1894.
[19] X.H. Cao, J.H. Li, M.J. Yang, et al., Macromol. Rapid Commun. 41 (2020) 1900622.
[20] C.J. Zhang, X.H. Cao, X.H. Zhang, Macromolecules 53 (2020) 203–211.
[21] B. Liu, H. Zhang, S. Liu, et al., Mater. Horiz. 7 (2020) 987–998.
[22] B. Liu, Y.L. Wang, W. Bai, et al., J. Mater. Chem. C 5 (2017) 4892–4898.
[23] B. Liu, B. Chu, Y.L. Wang, et al., Adv. Opt. Mater. 8 (2020) 1902176.
[24] X.H. Cao, C.J. Zhang, J.L. Yang, et al., Polym. Chem. 11 (2020) 309–314.
[25] M. Hou, Y. Zhong, L. Zhang, et al., Chin. Chem. Lett. 32 (2021) 1055–1060.
[26] Q. Jin, Y. Deng, X. Chen, J. Ji, ACS Nano 13 (2019) 954–977.
[27] J. Wang, H. Wang, H. Cui, et al., Chin. Chem. Lett. 31 (2020) 3143–3148.
[28] Q. Zhu, M. Saeed, R. Song, et al., Chin. Chem. Lett. 31 (2020) 1051–1059.
[29] X. Han, Y. Xu, M. Geranpayehvaghei, et al., Biomaterials 232 (2020) 119745.
[30] A. Zinger, L. Koren, O. Adir, et al., ACS Nano 13 (2019) 11008–11021.
[31] L. Hui, Y. Chen, Cancer Lett. 368 (2015) 7–13.
[32] X. Chen, H. Gao, Y. Deng, et al., ACS Nano 14 (2020) 5121–5134.
[33] L. Li, Y. Chen, W. Chen, et al., Chin. Chem. Lett. 30 (2019) 1689–1703.
[34] Y. Deng, P. Song, X. Chen, et al., ACS Nano 14 (2020) 9711–9727.
[35] J. Hu, X. Yuan, F. Wang, et al., Chin. Chem. Lett. 32 (2021) 1341–1347.
[36] H. Han, Y. Hou, X. Chen, et al., J. Am. Chem. Soc. 142 (2020) 4944–4954.
[37] X. Chen, F. Jia, Y. Li, et al., Biomaterials 246 (2020) 119999.
[38] D. He, Y. Tan, P. Li, et al., Chin. Chem. Lett. 32 (2021) 1743–1746.
[39] D. Hu, Y. Deng, F. Jia, et al., ACS Nano 14 (2020) 347–359.
[40] Y. Gao, J. Wang, M. Chai, et al., ACS Nano 14 (2020) 5686–5699.
[41] B. Schaible, T.Taylor T. Cormac, K. Schaffer, Antimicrob. Agents Chemother. 56 (2012) 2114–2118.
[42] D. Hu, L. Zou, W. Yu, et al., Adv. Sci. 7 (2020) 2000398.
[43] B.S. Zhao, I.A. Roundtree, C. He, Nat. Rev. Mol. Cell Bio. 18 (2017) 31–42.
[44] P. Boccaletto, M.A. Machnicka, E. Purta, et al., Nucleic Acids Res. 46 (2018) D303–D307.
[45] J.A. Bokar, M.E. Shambaugh, D. Polayes, et al., RNA 3 (1997) 1233–1247.
[46] J. Liu, Y. Yue, D. Han, et al., Nat. Chem. Biol. 10 (2014) 93–95.
[47] X.L. Ping, B.F. Sun, L. Wang, et al., Cell Res. 24 (2014) 177–189.
[48] G. Jia, Y. Fu, X. Zhao, et al., Nat. Chem. Biol. 7 (2011) 885–887.
[49] G. Zheng, John A. Dahl, Y. Niu, et al., Mol. Cell 49 (2013) 18–29.
[50] X. Wang, Z. Lu, A. Gomez, et al., Nature 505 (2014) 117–120.
[51] D. Dominissini, S. Moshitch-Moshkovitz, S. Schwartz, et al., Nature 485 (2012) 201–206.
[52] Kate D. Meyer, Y. Saletore, P. Zumbo, et al., Cell 149 (2012) 1635–1646.
[53] K. Chen, Z. Lu, X. Wang, et al., Angew. Chem. Int. Ed. 54 (2015) 1587–1590.
[54] B. Linder, A.V. Grozhik, A.O. Olarerin-George, et al., Nat. Methods 12 (2015) 767–772.
[55] K.D. Meyer, Nat. Methods 16 (2019) 1275–1280.
[56] Z. Zhang, L.Q. Chen, Y.L. Zhao, et al., Sci. Adv. 5 (2019) eaax0250.
[57] M.A. Garcia-Campos, S. Edelheit, U. Toth, et al., Cell 178 (2019) 731–747.
[58] X. Shu, J. Cao, M. Cheng, et al., Nat. Chem. Biol. 16 (2020) 887–895.
[59] D. Rus, M.T. Tolley, Nature 521 (2015) 467–475.
[60] H. Shahsavan, A. Aghakhani, H. Zeng, et al., Proc. Natl. Acad. Sci. U. S. A. 117 (2020) 5125.
[61] Y. Zhao, C. Xuan, X. Qian, et al., Sci. Robot. 4 (2019) eaax7112.
[62] X. Liu, J. Liu, S. Lin, X. Zhao, Mater. Today 36 (2020) 102–124.
[63] C. Wang, L. Xu, Y. Qiao, D. Qiu, Chin. Chem. Lett. 31 (2020) 821–825.
[64] B. Sui, Y. Li, B. Yang, Chin. Chem. Lett. 31 (2020) 1443–1447.
[65] C. Xian, Q. Yuan, Z. Bao, et al., Chin. Chem. Lett. 31 (2020) 19–27.
[66] Q.L. Zhu, C. Du, Y. Dai, et al., Nat. Commun. 11 (2020) 5166.
[67] Q.L. Zhu, C.F. Dai, D. Wagner, et al., Adv. Mater. 32 (2020) 2005567.
[68] Y.S. Kim, M. Liu, Y. Ishida, et al., Nat. Mater. 14 (2015) 1002–1007.
[69] Z. Sun, Y. Yamauchi, F. Araoka, et al., Angew. Chem. Int. Ed. 57 (2018) 15772–15776.
[70] D.P. Chang, J.E. Dolbow, S. Zauscher, Langmuir 23 (2007) 250–257.
[71] S. Palagi, A.G. Mark, S.Y. Reigh, et al., Nat. Mater. 15 (2016) 647–653.
[72] X.P. Hao, Z. Xu, C.Y. Li, et al., Adv. Mater. 32 (2020) 2000781.
[73] C.N. Zhu, C.Y. Li, H. Wang, et al., Adv. Mater. 33 (2021) 2008057.
[74] A. Sydney Gladman, E.A. Matsumoto, R.G. Nuzzo, et al., Nat. Mater. 15 (2016) 413–418.
[75] A. Zhang, F. Wang, L. Chen, et al., Chin. Chem. Lett. 32 (2021) 2923–2932.
[76] W. Yuan, X. Qu, Y. Lu, et al., Chin. Chem. Lett. 32 (2021) 2021–2026.
[77] H.C. Yu, S.Y. Zheng, L. Fang, et al., Adv. Mater. 32 (2020) 2005171.
[78] P. Payamyar, B.T. King, H.C. Öttinger, A.D. Schlüter, Chem. Commun. 52 (2016) 18–34.
[79] Z. Lin, Y. Liu, U. Halim, et al., Nature 562 (2018) 254–258.
[80] J.W. Colson, W.R. Dichtel, Nat. Chem. 5 (2013) 453–465.
[81] M. Paczuski, M. Kardar, D.R. Nelson, Phys. Rev. Lett. 60 (1988) 2638–2640.
[82] X. Wen, C.W. Garland, T. Hwa, et al., Nature 355 (1992) 426–428.
[83] C.F. Schmidt, K. Svoboda, N. Lei, et al., Science 259 (1993) 952–955.
[84] M.S. Spector, E. Naranjo, S. Chiruvolu, J.A. Zasadzinski, Phys. Rev. Lett. 73 (1994) 2867–2870.
[85] A.R. Koltonow, C. Luo, J. Luo, J. Huang, ACS Omega 2 (2017) 8005–8009.
[86] P. Li, S. Wang, F. Meng, et al., Macromolecules 53 (2020) 10421–10430.
[87] Y. Wang, S. Wang, P. Li, et al., Matter 3 (2020) 230–245.
[88] Y. Jiang, Y. Wang, Z. Xu, C. Gao, Acc. Mater. Res. 1 (2020) 175–187.
[89] J. Cao, X. Zhao, J. Wang, et al., Chin. Chem. Lett. 31 (2020) 265–268.
[90] C. Ye, F. Zhang, X. Tan, et al., Chin. Chem. Lett. 31 (2020) 2507–2511.
[91] X. Pan, J. Ji, N. Zhang, M. Xing, Chin. Chem. Lett. 31 (2020) 1462–1473.
[92] X. Zhang, J. Miao, P. Zhang, et al., Chin. Chem. Lett. 31 (2020) 2305–2308.
[93] J. Hou, O. Inganäs, R.H. Friend, F. Gao, Nat. Mater. 17 (2018) 119.
[94] S. Li, C.Z. Li, M. Shi, H. Chen, ACS Energy Lett. 5 (2020) 1554–1567.
[95] Z.P. Yu, K. Yan, W. Ullah, et al., ACS Appl. Polym. Mater. 3 (2021) 60–92.
[96] C. Sun, R. Xia, H. Shi, et al., Joule 2 (2018) 1816–1826.
[97] X. Li, R. Xia, K. Yan, et al., Chin. Chem. Lett. 31 (2020) 1608–1611.
[98] X. Li, R. Xia, K. Yan, et al., ACS Energy Lett. 5 (2020) 3115–3123.
[99] D. Wang, R. Qin, G. Zhou, et al., Adv. Mater. 32 (2020) 2001621.
[100] W. Song, B. Fanady, R. Peng, et al., Adv. Energy Mater. 10 (2020) 2000136.
[101] H. Shi, R. Xia, G. Zhang, et al., Adv. Energy Mater. 9 (2019) 1970016.
[102] Y. Lin, J. Wang, Z.G. Zhang, et al., Adv. Mater. 27 (2015) 1170–1174.
[103] J. Yuan, Y. Zhang, L. Zhou, et al., Joule 3 (2019) 1140–1151.
[104] Q. Liu, Y. Jiang, K. Jin, et al., Sci. Bull. 65 (2020) 272–275.
[105] M. Luo, C. Zhu, J. Yuan, et al., Chin. Chem. Lett. 30 (2019) 2343–2346.
[106] D.N. Jiang, K.R. Yan, C.Z. Li, Acta Chim. Sin. 78 (2020) 1287–1296.
[107] F.X. Chen, R. Qin, R. Xia, et al., ACS Energy Lett. 5 (2020) 1771–1779.
[108] N. Yan, C. Zhao, S. You, et al., Chin. Chem. Lett. 31 (2020) 643–653.
[109] T.J. Wen, D. Wang, L. Tao, et al., ACS Appl. Mater. Interfaces 12 (2020) 39515–39523.
[110] C. He, Y. Li, Y. Liu, et al., J. Mater. Chem. A 8 (2020) 18154–18161.
[111] C. Wang, H. Dong, W. Hu, et al., Chem. Rev. 112 (2012) 2208–2267.
[112] P. He, H. Zhang, C. Xu, et al., Chin. Chem. Lett. 30 (2019) 903–905.
[113] H. Najafov, B. Lee, Q. Zhou, et al., Nat. Mater. 9 (2010) 938–943.
[114] G. Li, R. Zhu, Y. Yang, Nat. Photonics 6 (2012) 153–161.
[115] A.C. Jakowetz, M.L. Bohm, A. Sadhanala, et al., Nat. Mater. 16 (2017) 551–557.
[116] R. Wu, B. Peng, H. Li, H. Li, Chem. Mater. 33 (2021) 19–38.
[117] X. Gong, M. Tong, Y. Xia, et al., Science 325 (2009) 1665–1667.
[118] H. Li, H.L. Xin, D.A. Muller, L.A. Estroff, Science 326 (2009) 1244–1247.
[119] J. Ren, M. Niu, X. Guo, et al., J. Am. Chem. Soc. 142 (2020) 1630–1635.
[120] G. Yu, J. Gao, J.C. Hummelen, et al., Science 270 (1995) 1789–1791.
[121] A.A. Bakulin, A. Rao, V.G. Pavelyev, et al., Science 335 (2012) 1340–1344.
[122] N. Wang, W. Yang, S. Li, et al., Chin. Chem. Lett. 30 (2019) 1277–1281.
[123] Z.P. Yu, X. Li, C. He, et al., Chin. Chem. Lett. 31 (2020) 1991–1996.
[124] R. Saraf, A. Mathur, V. Maheshwari, ACS Appl. Mater. Interfaces 12 (2020) 25011–25019.
[125] Z. Wei, Y. Zhao, J. Jiang, et al., Chin. Chem. Lett. 31 (2020) 3055–3064.
[126] T. Zhu, Y. Yang, S. Zhou, et al., Chin. Chem. Lett. 31 (2020) 2249–2253.